Journal of Materials Chemistry A

ROYAL SOCIETY OF CHEMISTRY

PAPER

View Article Online
View Journal | View Issue

Cite this: J. Mater. Chem. A, 2024, 12, 19247

Photoelectrochemical water splitting by hematite boosted in a heterojunction with B-doped g-C_3N_4 nanosheets and carbon nanotubes†

Irfan Khan, *[a] Tímea Benkó,[a] Anita Horváth,[a] Shaohua Shen, *[b] Jinzhan Su,[b] Yiqing Wang,[b] Zsolt E. Horváth,[c] Miklós Németh,[a] Zsolt Czigány,[c] Dániel Zámbó[c] and József Sándor Pap[a]

Received 11th April 2024
Accepted 1st June 2024

DOI: 10.1039/d4ta02512a

rsc.li/materials-a

Here, we effectively layered economically viable pyrolytic carbon nanotubes (p-CNTs) as solid-state mediators to accelerate the charge carrier transfer between hematite (α-Fe_2O_3) and boron-doped graphitic carbon nitride (B-C_3N_4). This synergistic combination leads to higher photoelectrochemical water splitting performance with a photoanodic current density of 2.85 mA cm^{-2}, which is a 4.1-fold enhancement compared to pristine α-Fe_2O_3 and the O_2 evolution rate detected was 22.70 μmol h^{-1} cm^{-2} with a Faraday efficiency of ~98% at 1.7 V_{RHE}. Mott–Schottky analysis confirms the highest donor density of 55.7 × 10^{19} cm^{-3} for the α-Fe_2O_3/B-C_3N_4/p-CNT photoanode, compared to α-Fe_2O_3 and α-Fe_2O_3/B-C_3N_4. Superstructuring the B-C_3N_4 and p-CNT onto pristine α-Fe_2O_3 enhances the charge separation and transfer efficiencies, and moreover mitigates recombination losses. DFT calculations suggest the type II charge transfer mechanism switched to an enhanced Z-scheme type by simple deposition of p-CNT on the α-Fe_2O_3/B-C_3N_4 heterojunction. Achieving such cost-effective, highly efficient hematite-based photoanodes offers an opportunity to fabricate tandem photoelectrochemical devices for low-cost solar fuel production.

Introduction

The harnessing of solar energy, an abundant and renewable natural resource, stands as the paramount solution to address the escalating global energy demands of our society. Photoelectrochemical (PEC) water splitting has garnered special attention, as this method generates hydrogen as a renewable energy carrier directly from sunlight, thus contributing to reducing our reliance on fossil fuels.[1–4] The oxygen evolution reaction (OER) with four-electron water oxidation is a crucial limiting factor both in the realm of electrochemical and photoelectrochemical water splitting.[5–7] It converts water to oxygen molecules at the anode following a multistep mechanism that involves surface oxygen species, O–O bond formation, and dioxygen release. Among the different steps, the O–O bond formation exhibits the highest activation energy barrier and thus is generally considered as the rate-limiting step. In PEC water splitting, the high kinetic barrier can be mitigated by increasing the reactivity of the intrinsic surface states of semiconducting materials, or by introducing co-catalysts, aiding in active site formation. Consequently, there has been a concerted effort to develop high-efficiency photoanodes for the OER.[8–10]

Metal-oxide semiconductors, including ZnO, WO_3, $BiVO_4$, and α-Fe_2O_3 (hematite), have emerged as promising candidates for photoanodes.[11–14] Hematite, in particular, is under intensive investigation due to its abundance in nature, environmental friendliness, high photochemical stability, and a narrow bandgap of 1.9–2.2 eV.[15] Despite these favorable properties, α-Fe_2O_3 faces challenges such as a short excited-state lifetime (~10^{-12} s),[16] poor OER kinetics,[17] limited hole diffusion,[18] and subpar electrical conductivity,[19] leading to significant electron–hole recombination in the bulk, interfaces, and surfaces, thereby limiting PEC efficiency.

Various strategies have been employed to overcome the limitations of hematite, including heterojunction construction,[20] doping with metals and nonmetals,[21–23] morphology advancement,[24] and co-catalyst loading.[25,26] Among these, forming nanoscale heterojunctions by coupling α-Fe_2O_3 with a second semiconductor has proven effective, leveraging appropriate bandgap overlap and enhanced charge separation at the junction interfaces. The charge transfer pathway in the heterostructure can either be a type II heterojunction or Z-scheme pathway, depending on the arrangements of band-

[a]Department of Surface Chemistry and Catalysis, HUN-REN Centre for Energy Research, Konkoly-ThegeM. Street 29-33, Budapest, 1121, Hungary. E-mail: irfan.khan@ek.hun-ren.hu

[b]International Research Center for Renewable Energy (IRCRE), State Key Laboratory of Multiphase Flow in Power Engineering (MFPE), Xi'an Jiaotong University, Xi'an, China

[c]HUN-REN Centre for Energy Research, Institute of Technical Physics and Materials Science, Konkoly-Thege M. Street 29-33, Budapest, 1121, Hungary

† Electronic supplementary information (ESI) available. See DOI: https://doi.org/10.1039/d4ta02512a

positions and Fermi-levels of the components.[27–29] The type-II heterojunction can efficiently promote excitons with less recombination; however, the high redox potential of the photocatalyst is sacrificed. Alternatively, the Z-scheme heterojunction retains a higher redox potential and minimizes recombination by using a mediator to transfer electrons from one semiconductor to another. This way, mediators can enhance the lifetime of charge carriers, leading to improved efficiency.[30,31]

Graphitic carbon nitride (g-C_3N_4) as a metal-free inorganic semiconductor exhibits suitable band potentials for water oxidation and is resistant to photocorrosion, making it suitable as a junction catalyst for α-Fe_2O_3 modification.[32–34] However, bulk g-C_3N_4 has high-rate recombination of photoinduced charges, and lower visible light absorbance due to its relatively large bandgap of ~2.72 eV that limits its photocatalytic activity.[35,36] Doping g-C_3N_4 with less electronegative elements, such as boron (B, giving B-C_3N_4), has emerged as an efficient strategy not only to improve absorption by narrowing the band gap of g-C_3N_4, but also to promote the photogenerated carrier separation due to the formation of a mid-gap state.[37–39] Additionally, materials such as CdS, MoS_2, CdSe, and Cu_2O are being explored for their potential in heterostructures with g-C_3N_4, operating *via* type-II, S-scheme, or Z-scheme mechanisms to enhance hydrogen evolution *via* efficient charge separation and solar energy utilization.[40–44]

A further issue may emerge from the transfer of charge carriers which is strongly influenced by the quality of interfacial contact between different particles. In this context, carbon nanotubes (CNTs) serve as useful additives due to their high surface area and excellent electrical conductivity.[45] In a heterojunction, CNTs can facilitate efficient charge carrier transport from the photoexcited α-Fe_2O_3 and g-C_3N_4, thereby suppressing recombination.

In contrast to previous anode functionalization methods that rely on single-component modifications, the integration of B-C_3N_4 and p-CNTs represents a significant advancement in heterojunction engineering. By leveraging the unique properties of each component, this sophisticated architecture optimizes charge carrier dynamics and redox capability. While controlled doping has been a challenge in previous photoanodes, optimized boron doping in g-C_3N_4 improves electrical conductivity and light absorption, generating higher charge carrier densities. Considering the distinctive properties of CNTs and boron-doped g-C_3N_4, the design of a heterojunction between an appropriate semiconductor and conductor has emerged as an effective strategy to enhance the photocatalytic ability of α-Fe_2O_3.

To our knowledge, our work is the first demonstration of a ternary α-Fe_2O_3/B-C_3N_4/CNT photoanode system for water splitting without additional sacrificial oxidants at neutral pH under visible light irradiation. We investigated the phase structure, chemical composition, morphology, and visible light-driven water-splitting activity. The type II heterojunction between the α-Fe_2O_3 and B-C_3N_4 is switched to an enhanced Z-scheme by using CNT. A further, unique feature of our ternary system is that the source of CNT is methane pyrolysis that itself produces turquoise H_2 and economically viable pyrolytic CNT (p-CNT hereafter) as a CO_x-free side-product.[46] We could utilize the p-CNT as a versatile conductor material for enhancing the redox capability of the hematite photoanode for the OER. Furthermore, we employed computations to confirm the interfacial band positions at the α-Fe_2O_3/B-C_3N_4 and the α-Fe_2O_3/B-C_3N_4/CNT interfaces. Such insights into charge transfer kinetics were often missing in earlier photoanode studies.

Experimental

Synthesis procedures

Synthesis of α-Fe_2O_3 nanorods. α-Fe_2O_3 nanorods (NRs) on titanium (Ti) substrates were synthesised by a straightforward wet chemical method. Initially, Ti sheets (1.5 × 2 cm) underwent a thorough cleaning process involving immersion in conc. HCl for 24 hours, followed by rinsing with acetone, ethanol, and ultrapure water. The cleaned sheets were immersed in a solution of 0.15 M $FeCl_3 \cdot 6H_2O$ and 1 M $NaNO_3$ at pH 1.5. This solution was then kept at 98 °C for 24 hours in an oven. The resulting sheets were annealed in air at 600 °C for 1 hour and allowed to cool naturally to room temperature (RT). This process yielded α-Fe_2O_3 nanorods grown onTi substrates.

Synthesis of boron doped g-C_3N_4 nanosheets. Ultrathin g-C_3N_4 nanosheets were synthesized by our previously reported thermal polymerization method, followed by a two-step ultrasonication–calcination technique.[47] Initially, melamine was placed in a covered alumina crucible and calcined at 520 °C in air for 4 hours (heating rate of 5 °C min^{-1}). The obtained yellow bulk g-C_3N_4 was dispersed in water and subjected to ultrasonication with stirring for 2 hours. Centrifugation of a suspension that was freeze-dried for 24 hours yielded a powder further calcined at 520 °C in air for 4 hours, yielding ultrathin g-C_3N_4 nanosheets. To synthesize B-C_3N_4, three batches of ultrathin g-C_3N_4 nanosheets were ground with $NaBH_4$. The resulting mixtures were then calcined at temperatures of 350, 450, and 550 °C in a nitrogen atmosphere for 1 hour (heating rate 10 °C s^{-1}). The powder was washed at RT multiple times with ethanol and deionized water to eliminate any residual $NaBH_4$. The brown-coloured B-C_3N_4 powder was obtained *via* freeze-drying. The B-C_3N_4 samples were denoted according to the calcination temperature as B-C_3N_4-350 °C, B-C_3N_4-450 °C, and B-C_3N_4-550 °C. Furthermore, the XRD pattern of these samples matched the expected diffraction peaks at 13.1° and 27.5° (Fig. S1†), particularly those corresponding to the (100) and (002) planes of g-C_3N_4, as we reported earlier.[47] It should be noted that the intensity of the (002) reflection is sensitive to the extent of ordered structures within the g-C_3N_4 framework.[48–50] These peaks signify the in-plane structural packing motif and interlayer stacking of aromatic systems, affirming the lack of discernible impurities.[51]

Synthesis of pyrolytic carbon nanotubes. Carbon nanotubes without any purification were obtained from a catalytic methane decomposition reaction (methane pyrolysis) carried out at 800 °C on supported NiMo/MgO catalysts as reported in our recent research.[46] Be aware that the thin, multiwalled carbon nanotubes may contain a limited amount of spent

$MoNi_{1.2}$ catalyst sample used to decompose methane.[46] These carbon nanotubes are referred to as p-CNTs, signing that they were obtained as precious by-products of pure, CO_x-free H_2 production from methane and subsequently utilized further in these photocatalytic experiments.

Synthesis of α-Fe_2O_3/B-C_3N_4 and α-Fe_2O_3/B-C_3N_4/p-CNT photoanodes *via* the drop casting technique. An aqueous suspension of 3 mg mL^{-1} B-C_3N_4 was prepared and subjected to ultrasonication in a bath for 2 h. Subsequently, 20 μL of this prepared dispersion was carefully drop-cast onto a pristine α-Fe_2O_3 photoanode and allowed to naturally dry, resulting in what we refer to as the α-Fe_2O_3/B-C_3N_4 photoanode. The fabricated photoanode underwent annealing in air at varying temperatures (350 °C, 450 °C, and 550 °C) that were adjusted to match the calcination temperatures for the B-C_3N_4 samples, with a controlled heating rate of 5 °C min^{-1}. For the preparation of the carbon nanotube-modified photoanode (α-Fe_2O_3/B-C_3N_4/p-CNT), an aqueous suspension containing both B-C_3N_4 (3 mg mL^{-1}) and p-CNT (0.2 mg mL^{-1}) mixed in equal volumes (1 mL each) in a separate plastic vial was used. This mixture underwent ultrasonication for 2 hours to ensure thorough dispersion. Subsequently, 20 μL of the prepared mixture was drop-cast onto the pristine α-Fe_2O_3 photoanode and allowed to air-dry naturally, denoted as α-Fe_2O_3/B-C_3N_4/p-CNT photoanode. Finally, the resulting composite photoanode was subjected to annealing in air at a temperature of 450 °C, using a controlled heating rate of 5 °C min^{-1} prior to catalytic experiments.

Sample characterization

X-ray diffractograms (XRD). X-ray diffractograms (XRD) were obtained using a D8 Discover diffractometer (Bruker AXS, Karlsruhe, Germany) with Cu Kα ($\lambda = 1.5406$ Å) radiation to analyze the crystallinity of the samples. The scan rate was set at 0.2° min^{-1}, with a 2θ step size of 0.02°. The X-ray beam dimensions were 1×5 mm^2. Phase identification was facilitated using the Diffrac. EVA program along with the ICDD PDF database.

Scanning electron microscopy (SEM). Scanning electron microscopy (SEM) investigations were conducted using a Thermo Scientific Scios2 dual-beam system (Waltham, MA, USA) equipped with an Oxford X-maxN 20 SDD EDX. A beam energy of 5 keV and a beam current ranging from 0.1 to 0.2 nA were applied in OptiTilt mode to achieve high-resolution secondary electron images. For elemental analyses by EDX, 2 keV and 1.6 nA were utilized to ensure surface sensitivity and high characteristic X-ray yield, respectively.

Transmission electron microscopy (TEM). Transmission electron microscopy (TEM) revealed the morphology and microstructure of the samples used in high-resolution TEM and high-angle annular dark-field (HAADF) modes. A Thermo-Fischer Themis 200 kV spherical aberration (Cs)-corrected TEM with 0.09 nm HRTEM and 0.16 nm STEM resolution was employed. STEM-EDS was utilized for composition analysis, and elemental maps were generated *via* spectrum imaging using 4 "Super X G1" EDS detectors integrated into the microscope. Cross-sectional lamellae of α-Fe_2O_3 nanorods for TEM examination were prepared using the Ga^+ Focused Ion Beam (FIB) of the Thermo Scientific Scios 2 scanning electron microscope. The nanorods were detached from the titanium substrate and dispersed onto a carbon-coated TEM grid.

X-ray photoelectron spectroscopy (XPS). X-ray photoelectron spectroscopy (XPS) measurements were carried out using a Kratos Axis Nova X-ray photoelectron spectrometer with monochromated Al Kα as the X-ray source. C 1s was used as the energy reference (284.6 eV) at a working current and potential of 10 mA and 15 kV, respectively, to investigate the surface composition of the samples.

Diffuse reflectance ultraviolet-visible spectroscopy (UV-vis DRS). Diffuse reflectance ultraviolet-visible spectroscopy (UV-vis DRS) was carried out using a Cary 60 UV-vis spectrophotometer (Agilent Technologies Inc., USA) equipped with a lab sphere diffuse reflectance accessory.

Attenuated total reflectance infrared spectroscopy (ATR IR). Attenuated total reflectance infrared spectroscopy (ATR IR) was performed on a PerkinElmer Spectrum Two instrument, using a diamond ATR unit in the range of 4000–450 cm^{-1} (8 scans).

Photoluminescence (PL). Photoluminescence (PL) measurements were performed on an Edinburgh FS5 spectrofluorometer from Edinburgh Instruments Ltd. Powder samples were loaded into quartz holders and were measured in an SC-10 tilted front-face solid sample cassette. The excitation wavelength was set to 320 nm. Emission spectra were recorded in the wavelength range of 380–750 nm.

Photoelectrochemical tests

All electro- and photoelectrochemical tests were performed on a BioLogic SP-150 potentiostat by employing a three-electrode configuration in 0.1 M Na_2SO_4 aqueous solution (pH 7). The working, counter and reference electrodes were the prepared photoanodes, Pt and Ag/AgCl (standard KCl), respectively. The immersion area of the working electrode was fixed at 1.5 cm^2. A Xe lamp (Asahi Spectra MAX-303) with an incident light intensity set at 100 mW cm^{-2} (1 sun) adjusted on the working electrode surface was used as the light source. The linear sweep voltammetry (LSV) curves were measured at a voltage range of 0.4–1.8 V *vs.* the reversible hydrogen electrode (V_{RHE}) with a scanning rate of 2 mV s^{-1}. The charge separation efficiency (η_{sep}) was evaluated in an electrolyte solution containing 0.1 M Na_2SO_3 and the efficiency values were determined using the equation: $J_{sulfite}/J_{max} = \eta_{abs} \times \eta_{sep}$, where $J_{sulfite}$ is the photocurrent measured in Na_2SO_3. J_{max} is the max photocurrent available in our system, which is 5.63 mA cm^{-2}.

Mott–Schottky (MS) curves were acquired within the voltage range of 0.2–1.6 V_{RHE} under dark conditions with a frequency of 1 kHz. The measured potentials *vs.* Ag/AgCl were converted to the RHE scale according to the Nernst equation: $E_{RHE} = E_{Ag/AgCl} + 0.059pH + EAg/AgCl^{0}$.[52] Incident photon-to-current conversion efficiency (IPCE) values were calculated at 1.23 V_{RHE} using the following equation: IPCE (%) = $(1240 \times J)/(P \times \lambda)$, where J is the photocurrent density (mA cm^{-2}); P is irradiation intensity; and λ is the wavelength (nm) of the incident monochromic light, which is controlled by a monochromator (71SW151, SOFN Instruments Co., Ltd).

Electrochemical impedance spectroscopy (EIS) was performed in the potential range of 1.1–1.5 V_{RHE} to obtain the Nyquist plots in a 0.1 M Na_2SO_4 aqueous solution under 100 mW cm^{-2} irradiation in the range of 330–600 nm. A model circuit was fitted to the experimental data points by using the Z-fit BioLogic software and contained a solution resistance (R_S) and two embedded R_Q elements: the capacitance of the space charge layer (Q_{sc}), the charge transfer capacitance (Q_{ct}) and the corresponding resistance of the space charge layer (R_{sc}), and the charge transfer (R_{ct}).

The O_2 evolution was measured using an Ocean Optics NeoFox probe, which was 2-point calibrated at 25 °C in the electrolyte saturated with argon (0% O_2) and air (20.9% O_2) prior to the photoelectrolysis experiments. The calibrated probe was immersed into the electrolyte during the photoelectrolysis experiments near the surface of the working electrode in a cell that was saturated with air, sealed and thermostatted.

DFT calculations

First-principles density functional theory (DFT) calculations were performed using the CASTEP code.[53] The exchange–correlation effects were treated within generalized gradient approximation (GGA) with the Perdew–Burke–Ernzerhof (PBE) potential.[54] The interaction between the ionic core and valence electrons was simulated by the ultrasoft pseudopotentials.[55] The van der Waals interaction was considered by using the empirical correction in TS (Tkatchenko and Scheffler).[56] The kinetic energy cutoff was chosen to be 500 eV. Brillouin zone integration was sampled with $5 \times 5 \times 1$ and $4 \times 5 \times 1$ Monkhorst–Pack mesh *K*-points for the calculation. The slabs were set by a vacuum region of 30 Å. The structures are allowed to be fully relaxed and optimized until convergence to 10^{-5} eV in total energy and 0.01 eV $Å^{-1}$ in the forces.

Results and discussion

XRD analysis

The crystalline structure of the samples was examined by XRD, as illustrated in Fig. 1. The diffraction pattern of the Ti-sheet, incorporating iron-oxide, reveals the presence of seven distinct peaks corresponding to α-Fe_2O_3 crystals (PDF #01-087-1164), exhibiting a rhombohedral geometry. Simultaneously, Ti diffraction peaks (PDF #00-044-1294) point to the possible integration interface of α-Fe_2O_3 nanorods with the Ti-sheet. This outcome is indicative of a controlled synthesis process and the nature of the produced back interface material phase.[57] Notably, the characteristic reflection of B-C_3N_4 in α-Fe_2O_3/B-C_3N_4 at $2\theta = 27.5°$ for the (002) plane did not allow unambiguous phase characterization by XRD, because of its low amount relative to the bulk phase and the overlap with the (110) reflection of rutile. Instead, we relied on TEM, XPS and ATR-IR analysis of the surface, showing a homogeneous distribution of the B-C_3N_4-associated elements on the surface of α-Fe_2O_3. It is essential to highlight that despite surface modifications with B-C_3N_4 and p-CNT, the lattice structure of the hematite crystal system remains unchanged. This observation may be attributed to the limited loading amount of B-C_3N_4 and p-CNT on the pristine hematite surface, as reported in the literature.[58,59]

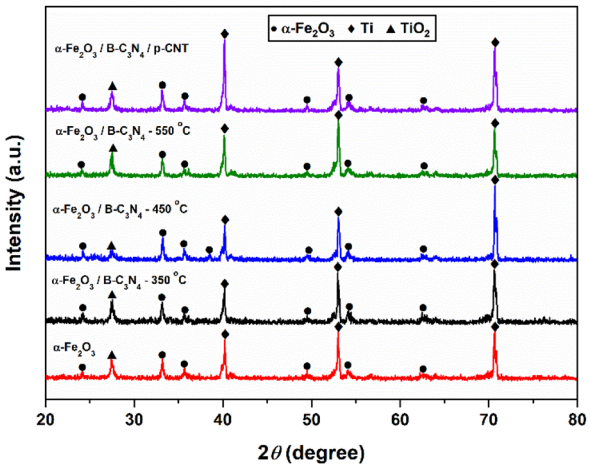

Fig. 1 XRD patterns of the α-Fe_2O_3, α-Fe_2O_3/B-C_3N_4 and α-Fe_2O_3/B-C_3N_4/p-CNT used photoanodes.

Morphological analysis

The morphological characteristics of both pristine and modified hematite samples exposed to PEC conditions were investigated by SEM (Fig. 2a and b). The SEM analysis unveiled that the pristine α-Fe_2O_3 synthesized on the Ti-substrate exhibited a distinct nanorod morphology (Fig. 2a), while the introduction of B-C_3N_4 did not impose discernible alterations on the overall morphology of hematite (Fig. 2b). Notably, high-resolution SEM imaging delineated these uniform nanorods with a diameter of 50–60 nm and a length of approximately 500 nm subsequent to annealing at 550 °C.

Furthermore, the HRTEM analysis of the used α-Fe_2O_3/B-C_3N_4 composite (Fig. 2c) revealed a lattice spacing of 0.25 nm (Fig. 2c, inset), assigned to the (110) plane of α-Fe_2O_3 that is identical to the pristine sample. In the corresponding SAED pattern (Fig. 2d), the reflections could be associated with hematite, but no reflections from B-C_3N_4 could be identified. Indeed, further images in Fig. 2c and S2a† delineate only amorphous structures on the α-Fe_2O_3 surface (indicated by an arrow). While such nanostructures are often associated with g-C_3N_4 nanosheets and CNTs in existing literature,[60–64] we concluded that our TEM images did not substantiate such assertions.

To elucidate the phase analysis of the B-C_3N_4 ad-layer, we conducted lower-resolution TEM imaging on the as-prepared α-Fe_2O_3/B-C_3N_4 composite nanorods. This imaging revealed a distinct *ca.* 3 nm thick B-C_3N_4 overlayer on some nanorods (Fig. 2e). However, detailed statistical analysis was beyond this study's scope. Notably, at HRTEM conditions the B-C_3N_4 layer was beam sensitive which led to the destruction of the B-C_3N_4 layer on hematite. This was evident when attempts to examine the lattice fringes of the overlayer in Fig. 2e using HRTEM proved unsuccessful. Upon reverting to lower magnification, the overlayer was no longer visible.

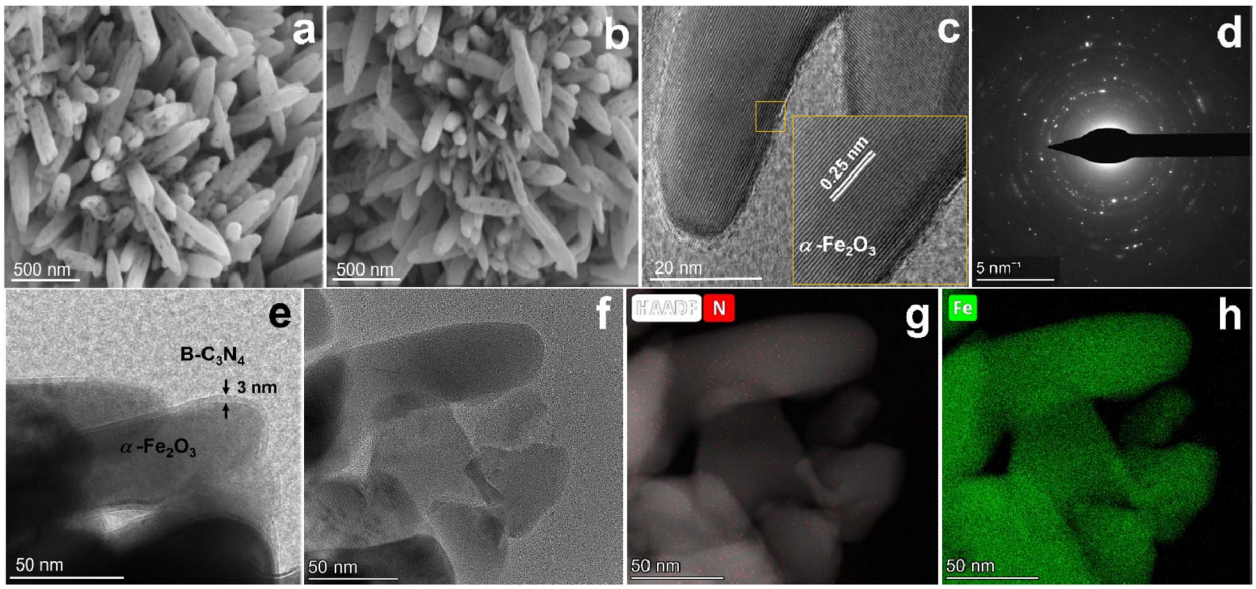

Fig. 2 (a) Top-view SEM images of the used α-Fe_2O_3 and (b) α-Fe_2O_3/B-C_3N_4 photoanodes at 50 000× magnification; (c) HRTEM image of α-Fe_2O_3 nanorods and (d) SAED pattern of the used α-Fe_2O_3/B-C_3N_4 photoanode; the inset shows an enlarged area and the lattice fringes (yellow square); (e) TEM image of an as-prepared α-Fe_2O_3/B-C_3N_4 nano-assembly showing the interface formed between the two components; (f) TEM image and (g) HAADF including N map and (h) Fe elemental map of the same area of the used α-Fe_2O_3/B-C_3N_4/p-CNT photoanode.

Therefore, XPS spectra were meticulously analysed (detailed in the subsequent section) to validate the presumption that nanorods are covered with B-C_3N_4. HAADF and STEM-EDS images (Fig. 2g–h, nitrogen mapping) provided evidence supporting the effective surface decoration of ultrathin B-C_3N_4 onto the α-Fe_2O_3 nanorods. Further, supplementation from STEM-EDS images (Fig. S2c–e†) of the α-Fe_2O_3/B-C_3N_4/p-CNT composite showcased a homogeneous distribution of nitrogen (N), iron (Fe) and oxygen (O) species across the entirety of the nanorod structures, thereby affirming the successful integration of B-C_3N_4 onto α-Fe_2O_3.

XPS analysis

The obtained XPS spectra, as depicted in Fig. 3, on samples with confirmed PEC activity (discussed later) affirm the expected elements on the surface of α-Fe_2O_3, α-Fe_2O_3/B-C_3N_4 and α-Fe_2O_3/B-C_3N_4/p-CNT (Table S1† contains the atomic ratios) emphasizing the comprehensive nature of the nanocomposites in the latter two cases. The Fe 2p doublet at 711.1 and 724.5 eV provides crucial insights into the oxidation state of Fe in pristine α-Fe_2O_3, confirming the +3 oxidation state.[65,66] Importantly, the Fe 2p spectra, with only minimal variations, suggest that the incorporation of B-C_3N_4 and p-CNT has negligible effects on the electronic structure and charge properties of hematite. This observation is consistent with literature findings, reinforcing the stability of hematite's electronic structure under the influence of these additives.[67–69] The N 1s peak at 397.5 eV belongs to the N–B species and the peak at 398.0 eV is attributed to sp^2 nitrogen, specifically the C–N=C bond of graphitic carbon nitride.[70,71] Additionally, the peak at 400.1 eV is assigned to the sum of this adventitious nitrogen and the N–C3 component of the graphitic carbon nitride in B-C_3N_4 containing samples.[72–74] This identification contributes to a more detailed understanding of the nitrogen species present in the composite, emphasizing the role of B-C_3N_4 in introducing specific nitrogen functionalities. The O 1s peak resolved to sub-peaks at 530.1, 532.5, and 532.7 eV is associated with Fe–O bonds, oxygen vacancies, and water, respectively.[75] Importantly, the absence of a noticeable shift in the Fe–O binding energy within the O 1s spectra further corroborates the structural stability of the nanocomposite. Additionally, the C 1s peak at 288.1 eV is ascribed to sp^2-hybridized carbon in heterocycles (N–C=N).[76,77] The rest of the peaks at 284.9, 286.4 and 288.7 eV are due to adventitious carbon contaminants, mostly hydrocarbons with C–C and C–H bonds, but also some oxygenated functional groups like C–O, C=O and O–C=O.[78–80]

Consistency across measurements taken at three different spots, each with a diameter of around 0.9 mm, indicates homogeneous surfaces, reinforcing the reliability and reproducibility of the results. These XPS findings, in conjunction with XRD and elemental mapping, collectively validate the successful decoration of B-C_3N_4 on the hematite surface, providing a comprehensive characterization of the nanocomposite's structural and compositional attributes.

ATR-IR analysis

To further confirm the presence of B-C_3N_4 in the photoanodes, ATR-IR spectroscopy was employed (Fig. S3a†). For the as-synthesized B-C_3N_4-450 °C, the broad peak at 3000–3400 cm^{-1} is attributed to the N–H stretching vibration and the strong peak emerging at 2180 cm^{-1} corresponds to the asymmetric stretching vibration of cyano (N≡C–) groups.[81] The peaks in the 1100–1700 cm^{-1} region correspond to the C–N/C–C and C=N stretching modes of heterocyclic compounds (Fig. S3b†).[82,83] All

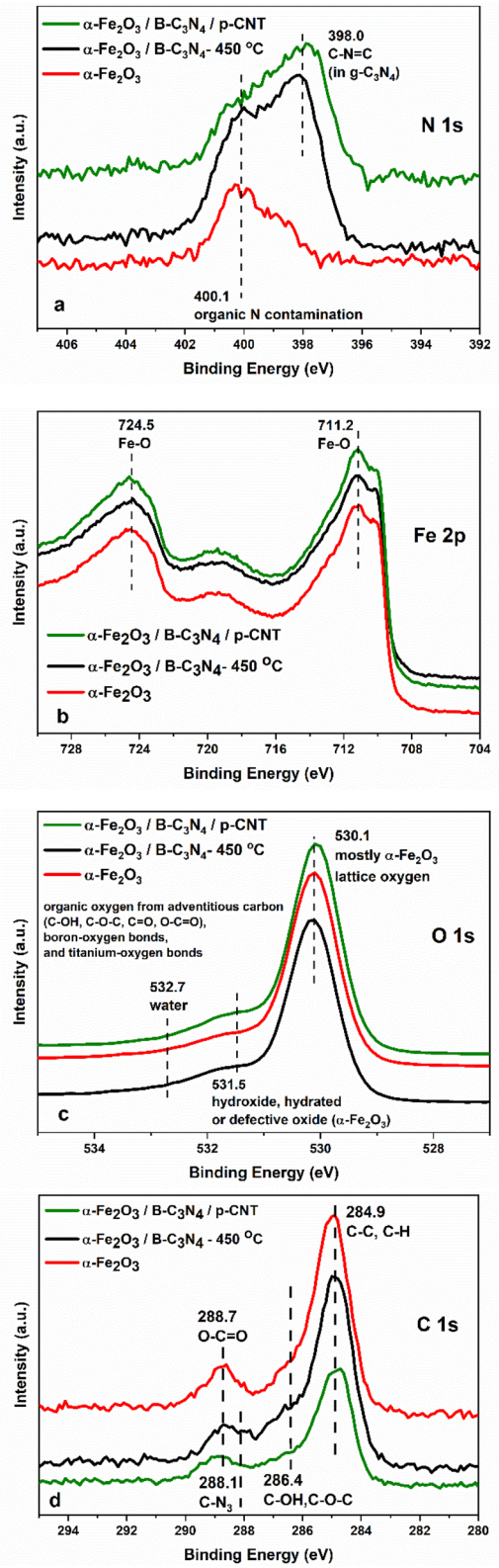

Fig. 3 (a) The N 1s, (b) Fe 2p, (c) O 1s and (d) C 1s XPS spectra of the used α-Fe_2O_3, α-Fe_2O_3/B-C_3N_4-450 °C, and α-Fe_2O_3/B-C_3N_4-450 °C/p-CNT photoanodes.

these characteristic absorption peaks of B-C_3N_4 and α-Fe_2O_3 were clearly present in the α-Fe_2O_3/B-C_3N_4 composite. This suggests that the original chemical structures of the individual components are preserved after the formation of the heterojunction. However, the intensity of the peaks was weak in α-Fe_2O_3/B-C_3N_4/p-CNT due to a very low amount being drop-cast onto the α-Fe_2O_3 surface, consistent with the XPS, XRD and TEM results. In the spectrum of α-Fe_2O_3, the absorption peak located at 524 cm^{-1} is associated with the stretching vibrations of the Fe–O bond.[62]

Performance in photoelectrochemical water splitting

The photoelectrochemical (PEC) activities of pristine α-Fe_2O_3, α-Fe_2O_3/B-C_3N_4, and α-Fe_2O_3/B-C_3N_4/p-CNT photoanodes were evaluated in detail to assess their efficacy in water splitting under visible light irradiation. The range of electrochemical stability has been explored by CV in the dark (Fig. S4†). Electron injection to the CB states of hematite limits the safe potential window roughly to 0.4 V_{RHE}. The VB states start to empty only beyond 2.0 V_{RHE}, whereas those of B-C_3N_4 start to empty beyond 1.8 V_{RHE}. The latter effect is intensified by the presence of p-CNT. Keeping the external bias beyond these thresholds induces irreversible adverse changes in the anodes. Note that the current peaks corresponding to the S2 state of α-Fe_2O_3 occur in case α-Fe_2O_3/B-C_3N_4/p-CNT is polarized to higher anodic potentials,[84] signalling effective electron transfer from α-Fe_2O_3 to p-CNT, as DFT predicts (*vide infra*).

The evaluation involved measuring the PEC response by LSV under chopped light irradiation (Fig. 4). Pristine α-Fe_2O_3 exhibited a relatively low photocurrent density limit of approximately 0.31 mA cm^{-2} at 1.23 V_{RHE}. In contrast, the addition of B-C_3N_4 under optimized annealing conditions enhanced the photocurrent density to around 0.71 mA cm^{-2} at 1.23 V_{RHE} for the α-Fe_2O_3/B-C_3N_4 photoanode. To assess the possible impact of TiO_2 (detected by XRD) on the PEC performance, LSV measurements were conducted using an uncoated Ti sheet, as shown in Fig. S5.† Although XRD confirmed the presence of TiO_2, the very low photocurrent density suggests that it has a negligible effect on the overall PEC water splitting performance.

Notably, the PEC performance was influenced by the annealing temperature during the deposition of B-C_3N_4 onto pristine hematite. As illustrated in Fig. 4a, there was a discernible increase in photocurrent density with the rise in annealing temperatures from 350 °C to 450 °C. However, surpassing this optimal temperature threshold to 550 °C resulted in a decline in the photocurrent. Note that the disruption of the B-C_3N_4 structures is expected to hinder the movement of charge carriers and limit the photocurrent activity. Such disrupted B-C_3N_4 structure may occur when the annealing temperature is elevated to 550 °C under air, inducing the observed decline in the photocurrent.

PL spectra of B-C_3N_4 samples were recorded to gain insight into the influence of heat treatment temperature on the charge carrier dynamics of this material (Fig. S6†). The results allowed us to conclude that the low intrinsic PL activity (a result of better

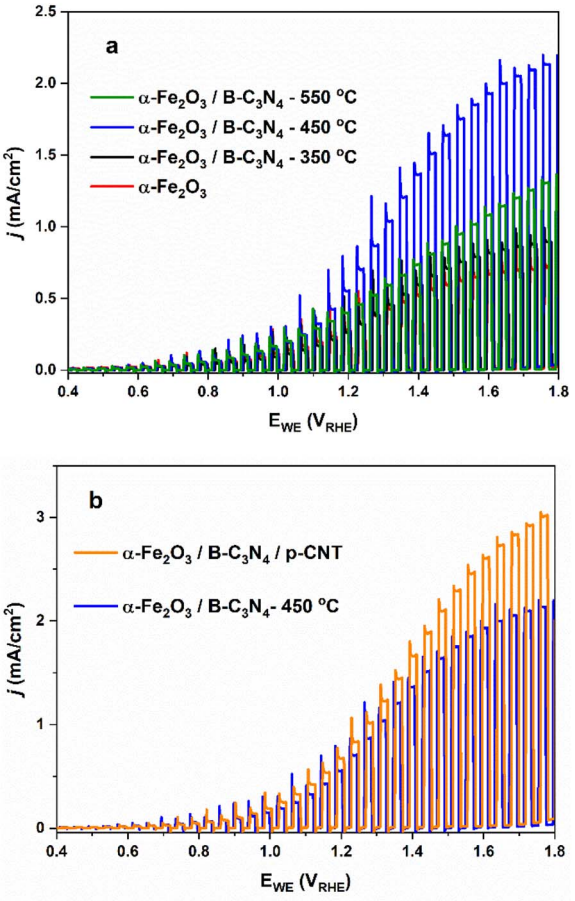

Fig. 4 (a) Linear sweep voltammetry plots of all the photoanodes; (b) comparative LSV plots between α-Fe_2O_3/B-C_3N_4-450 °C and α-Fe_2O_3/B-C_3N_4-450 °C/p-CNT obtained in 0.1 M Na_2SO_4 at pH 7.

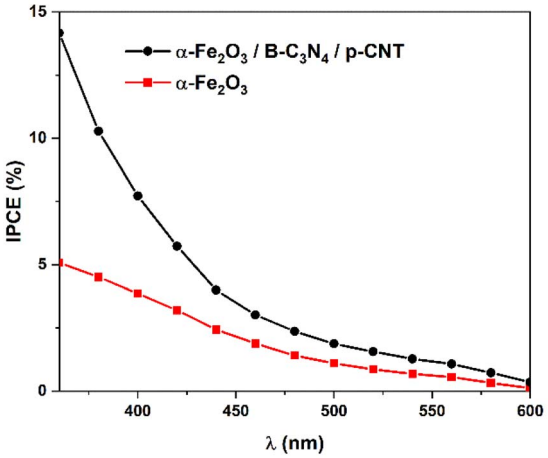

Fig. 5 IPCE curves of pristine and modified α-Fe_2O_3 photoanodes obtained in 0.1 M Na_2SO_4 at pH 7.

charge separation and PEC activity) of B-C_3N_4 is necessary but not sufficient for better PEC properties, when B-C_3N_4 is combined with hematite. Consequently, the post-annealing temperature was fixed at 450 °C for B-C_3N_4 decoration for subsequent measurements.

To further improve the PEC performance of the α-Fe_2O_3/B-C_3N_4 photoanode, economically viable p-CNT was deposited onto its surface using a simple drop-casting technique. Remarkably, the p-CNT served as a conductor, facilitating charge transfer between the α-Fe_2O_3 and B-C_3N_4 heterojunctions. The modified α-Fe_2O_3/B-C_3N_4-450 °C/p-CNT photoanode exhibited an even higher photocurrent density of approximately 2.85 mA cm^{-2} at 1.7 V_{RHE} (Fig. 4b), indicating a 4.1 times larger value than that of pristine α-Fe_2O_3.

Additional insight into the photocurrent generation was gained through IPCE measurements, which showed a clear wavelength dependence and corroborated with the increase in PEC performance (Fig. 5). Specifically, the IPCE increased from 5.0% for pristine α-Fe_2O_3 to 14.1% for α-Fe_2O_3/B-C_3N_4-450 °C/p-CNT. Moreover, the α-Fe_2O_3/B-C_3N_4-450 °C/p-CNT photoanode demonstrated chemical stability, maintaining its photocurrent density during a 1 hour controlled potential electrolysis in 0.1 M Na_2SO_4 at 1.7 V_{RHE} under 100 mW cm^{-2} illumination, as illustrated in Fig. S7.† These results not only highlight the superior PEC performance achieved, but also underscore the physical and chemical stability conferred by the B-C_3N_4 and p-CNT decoration on the surface of hematite.

The charge separation efficiency (η_{sep}) and charge transfer efficiency (η_{ct}) were determined by comparing the photocurrent in the presence and absence of 0.1 M Na_2SO_3 as a hole scavenger (Fig. 6a–c). This comparison is predicated on the notably greater thermodynamic driving force observed for sulfite oxidation (eqn (1)) compared to water oxidation (eqn (2)).

Due to the substantially higher thermodynamic potential associated with sulfite oxidation, η_{ct} is anticipated to approach maximum efficiency in the presence of SO_3^{2-}.

$$SO_3^{2-} + h^+ \rightarrow SO_3^{\bullet -},\ E^\circ = 0.75\ V_{RHE} \quad (1)$$

$$2H_2O + 4h^+ \rightarrow 4H^+ + O_2,\ E^\circ = 1.23\ V_{RHE} \quad (2)$$

Fig. 6a illustrates the LSV curves of the photoanodes in the presence of sulfite under chopped light irradiation. As anticipated, both pristine α-Fe_2O_3 and the α-Fe_2O_3/B-C_3N_4-450 °C/p-CNT composite exhibited enhanced photocurrent densities of 0.4 mA cm^{-2} and 1.1 mA cm^{-2}, respectively, at 1.23 V_{RHE}. The maximum photocurrent density of 4.8 mA cm^{-2} was reached at 1.80 V_{RHE}. This increase in photocurrent indicates improved hole transportation to the surface and rapid reaction with sulfite in α-Fe_2O_3/B-C_3N_4-450 °C/p-CNT compared to α-Fe_2O_3 alone. Fig. 6b reveals a lower η_{sep} of 5.5% calculated for pristine hematite, potentially due to high electron/hole recombination in bulk defect sites and poor electron transport.[85] Notably, a significantly enhanced η_{sep} of 10.1% at 1.23 V_{RHE} is observed for α-Fe_2O_3/B-C_3N_4-450 °C, suggesting that the decoration of B-C_3N_4 on the hematite surface remarkably inhibits charge recombination. Furthermore, the highest η_{sep} of 14.6% at 1.23 V_{RHE} exhibited by α-Fe_2O_3/B-C_3N_4-450 °C/p-CNT indicates a synergistic effect of B-C_3N_4 and p-CNT.

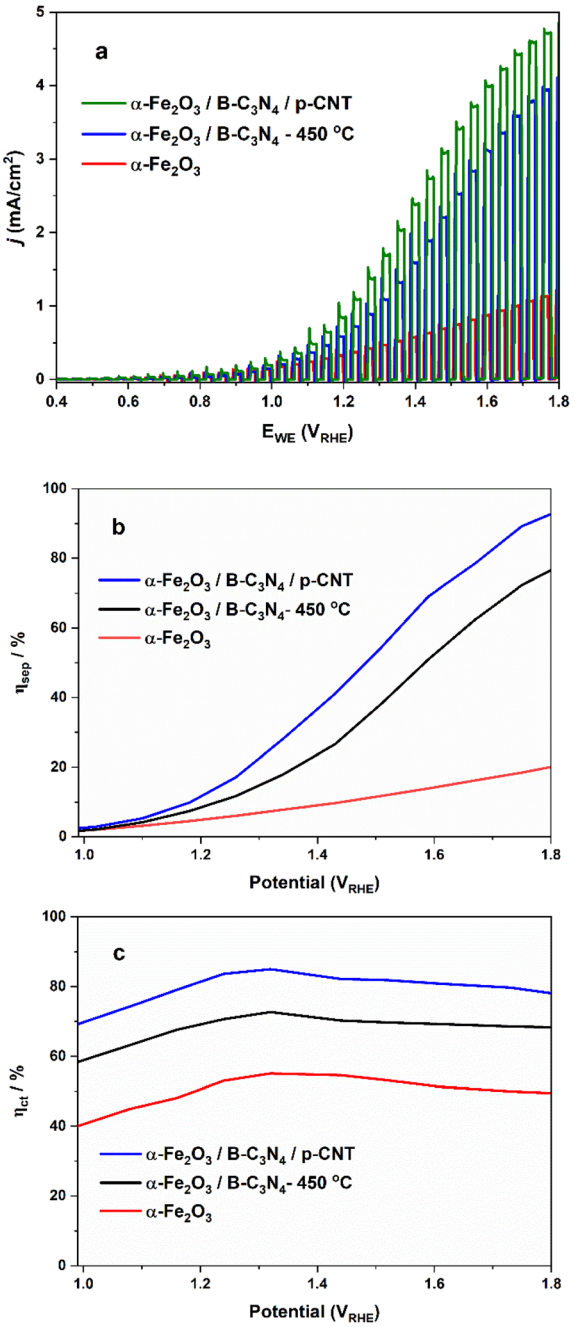

Fig. 6 (a) Linear sweep voltammetry plots of the photoanodes obtained in 0.1 M Na_2SO_3 at pH 7; (b and c) charge separation (η_{sep}) and charge transfer (η_{ct}) efficiency of the photoanodes.

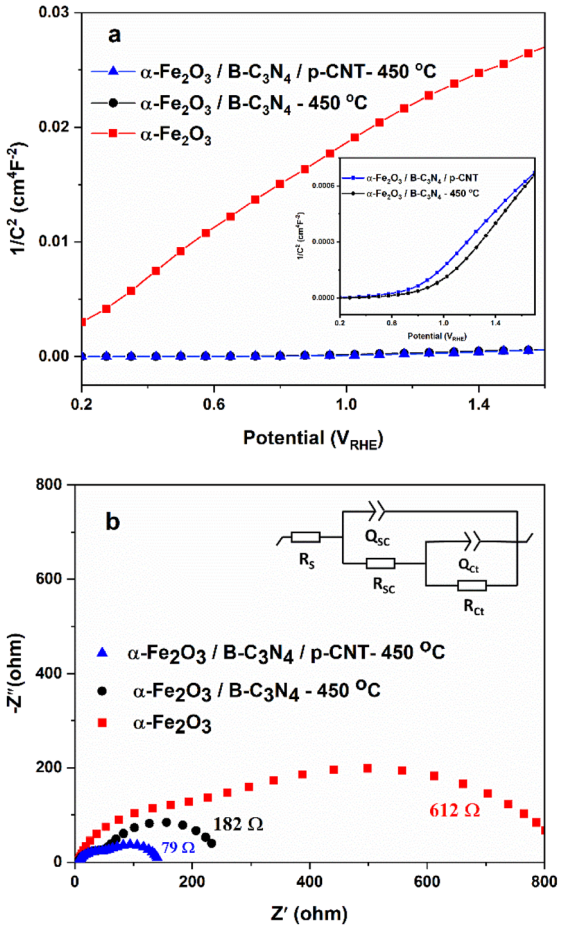

Fig. 7 (a) Mott–Schottky curves; (b) EIS Nyquist plots for the photoanodes; the inset of (a) shows the resolution view; the inset of (b) shows the equivalent circuit for EIS fitting.

To delve deeper into the charge transfer kinetics, Mott–Schottky (M–S) analysis was conducted, with the corresponding curves illustrated in Fig. 7a. The M–S plots provided notable insights into the semiconductor–electrolyte interface behavior. In the case of pristine α-Fe_2O_3, a flat band potential of approximately −0.04 V_{RHE} was observed that shifted to 0.77 V_{RHE} upon the introduction of B-C_3N_4. Furthermore, the carrier densities (N_d) were calculated using the reciprocal slopes of the M–S plots (Fig. 7a). For α-Fe_2O_3, α-Fe_2O_3/B-C_3N_4, and α-Fe_2O_3/B-C_3N_4-450 °C/p-CNT, the carrier densities were found to be 2.2×10^{19}, 52.4×10^{19}, and 55.7×10^{19} cm^{-3}, respectively.

The charge transfer efficiency of a photoanode determines the proportion of photogenerated holes transferred from the surface into the electrolyte. As depicted in Fig. 6c, η_{ct} remarkably increased from 51.4% to 70.1%, and even up to 83.7% at 1.23 V_{RHE} for α-Fe_2O_3, α-Fe_2O_3/B-C_3N_4-450 °C, and α-Fe_2O_3/B-C_3N_4-450 °C/p-CNT, respectively. This enhancement suggests that p-CNT plays a crucial role in facilitating charge transfer from the electrode surface to the electrolyte.

The considerable increase in carrier density upon the incorporation of B-C_3N_4, in addition to the large anodic shift in the flatband potential, indicates the pronounced role of B-C_3N_4 in facilitating carrier separation. This improved carrier separation subsequently leads to enhanced electrical conductivity, favours charge carrier migration towards the semiconductor–electrolyte interface and promotes more efficient PEC water oxidation. Interestingly, further decoration with p-CNT resulted in only a modest increment in carrier density. However, the enhanced PEC performance of α-Fe_2O_3/B-C_3N_4-450 °C/p-CNT compared to α-Fe_2O_3/B-C_3N_4-450 °C cannot solely be attributed to the increased carrier density. Instead, it is presumed

that the superior performance may arise from a suppressed charge carrier surface recombination. This suggests that while carrier density plays a significant role, other factors such as charge carrier recombination dynamics also contribute significantly to the overall PEC performance.

The charge transfer kinetics was further investigated by EIS. In Fig. 7b, Nyquist plots were generated for all photoanodes, revealing a distinctive two-semicircle pattern characteristic of such analyses.[86,87] Each semicircle in the plot corresponds to different charge transfer processes within the photoanode–electrolyte system. Specifically, the high-frequency semicircle reflects the internal charge transfer resistances within the bulk of the material (R_{sc}), while the low-frequency semicircle represents the charge transfer resistances at the interface between the photoanode and the electrolyte (R_{ct}). In the Nyquist plots presented, it is noteworthy that α-Fe_2O_3/B-C_3N_4-450 °C/p-CNT exhibits the smallest semicircle, indicating a significantly lower R_{ct} value (79 Ω) compared to those of both α-Fe_2O_3/B-C_3N_4-450 °C (182 Ω) and α-Fe_2O_3 (612 Ω). This improvement in charge transfer dynamics can be attributed to several factors. Firstly, the incorporation of B-C_3N_4 likely facilitates electron transfer pathways within the bulk of the α-Fe_2O_3 photoanode, thereby reducing R_{sc}. Secondly, the interfacial coordination between B-C_3N_4 and p-CNT likely promotes efficient electron transfer at the photoanode–electrolyte interface, minimizing R_{ct} and enabling more efficient exchange of charge carriers with the electrolyte.

Finally, the O_2 evolution rate for α-Fe_2O_3/B-C_3N_4-450 °C/p-CNT detected with an optical probe was 22.70 μmol h^{-1} cm^{-2} at 1.7 V_{RHE}, with a Faraday efficiency of ~98% (Fig. S7†), indicating a high degree of agreement between the measured and evolved concentrations of oxygen, further validating the efficacy of the composite photoanode.

Photocatalytic mechanism

On the basis of the above discussions, a possible mechanism for the synergistic effect of the B-C_3N_4 on the hematite surface involves the formation of a heterojunction, which is transformed to a double Z-scheme by p-CNT enhancing the overall photoelectrochemical activity. The optical absorption edges of α-Fe_2O_3 and B-C_3N_4-450 °C in the UV-vis absorption spectra are observed at approximately 590 and 450 nm, respectively. Tauc plots indicate band gaps of 2.10 eV for α-Fe_2O_3 and 2.04 eV for B-C_3N_4-450 °C (Fig. S8†). Due to the more negative conduction band (CB) of B-C_3N_4-450 °C and the more positive valence band edge potential (VB) of α-Fe_2O_3, a type II heterojunction is established.[88–90]

Results from DFT calculations further confirm this hypothesis by shedding light on the differential charge density within the α-Fe_2O_3/B-C_3N_4 structure. The calculations reveal that electronic interactions between α-Fe_2O_3 and B-C_3N_4 are notably weak. The holes and electrons are distributed on B-C_3N_4 and α-Fe_2O_3, respectively. Upon incorporating p-CNT into the α-Fe_2O_3/B-C_3N_4 framework, a significant transfer of interlayer electrons is observed in the α-Fe_2O_3/B-C_3N_4/p-CNT structure. This alteration prompts a redistribution of charge carriers, resulting in an enrichment of holes within both α-Fe_2O_3 and B-C_3N_4, while electrons predominantly occupy the p-CNT component.

This intriguing charge transfer mechanism piqued our research interest, prompting us to delve deeper into its intricacies. To facilitate our investigation, we initiated DFT calculations to determine the work functions of α-Fe_2O_3, B-C_3N_4, and p-CNT, which were found to be 5.18, 5.39, and 4.18 eV, respectively (Fig. S9† for details), based on the optimised structural model shown in Fig. 8a. The higher work function of B-C_3N_4 facilitates electron transfer to α-Fe_2O_3, while holes transfer from hematite to B-C_3N_4. This transfer is driven by the tendency of the system to reach an equilibrium state, equalizing Fermi levels at the α-Fe_2O_3/B-C_3N_4 heterojunction interface.

In detail, α-Fe_2O_3 exhibits a CB position of −5.0 eV and a VB position of −7.1 eV, while B-C_3N_4 has a CB position of −4.8 eV and a VB position of −6.7 eV. The Fermi level difference promotes the transfer of photoinduced electrons from B-C_3N_4 to the CB of α-Fe_2O_3 and the transfer of holes to the VB of B-C_3N_4, solidifying the formation of a type II heterojunction as shown in Fig. 8b.

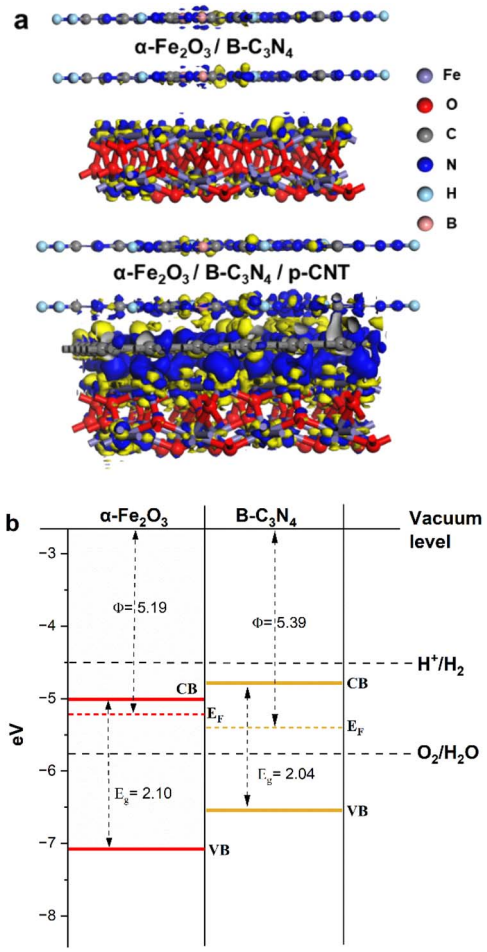

Fig. 8 (a) Side-view differential charge density map of α-Fe_2O_3/B-C_3N_4 and α-Fe_2O_3/B-C_3N_4/p-CNT. The iso-surface value is 0.016 e $Å^{-3}$. The yellow and blue regions represent net electron accumulation and depletion, respectively; (b) energy band diagram of the α-Fe_2O_3, B-C_3N_4 type II heterojunction, and p-CNT Fermi level before contact (numerical values are given in eV).

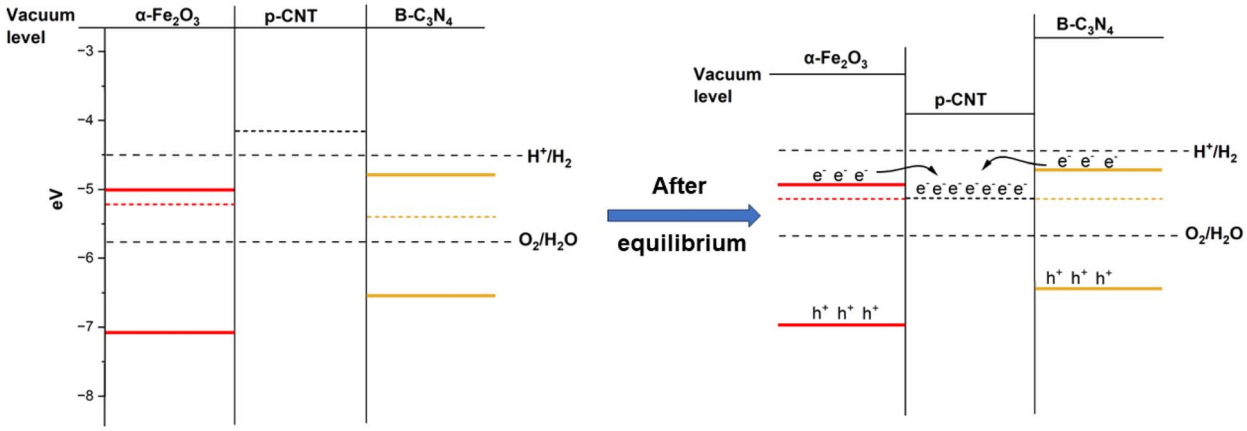

Fig. 9 Schematic energy levels of B-C_3N_4 and p-CNT decorated on the α-Fe_2O_3 photoanode.

Upon introducing p-CNT into the α-Fe_2O_3/B-C_3N_4 system, the subsequent formation of contacts becomes pivotal. The α-Fe_2O_3 and p-CNT first come into contact, with the higher Fermi energy level of p-CNT causing electrons to flow from α-Fe_2O_3 towards p-CNT, while α-Fe_2O_3 collects holes. A similar scenario occurs when B-C_3N_4 and p-CNT are in contact, altogether resulting in a double Z-type heterojunction (Fig. 9). Since p-CNT acts as an electron conductor, electrons are rapidly directed to the electrode support, expediting the photoelectrocatalytic reaction. This configuration promotes the formation of a Z-scheme structure for water splitting, a concept well-established in prior research.[64,91–94] Consequently, the introduction of p-CNT with its high conductivity enhances the efficient separation of charge carriers, culminating in the increased photoelectrochemical activity of the α-Fe_2O_3/B-C_3N_4-450 °C/p-CNT system.

Conclusions

This study demonstrates opportunities for utilizing pyrolytic carbon nanotubes (produced selectively in methane to hydrogen transformation) as a cost-effective and versatile conductive material for achieving high-performance PEC photoanodes. In this study, the integration of B-C_3N_4/p-CNT onto the surface of an α-Fe_2O_3 photoanode was accomplished through a straightforward drop-casting and annealing process. The resulting α-Fe_2O_3/B-C_3N_4-pCNT composite exhibited a notable 4.2-fold increase in photocurrent density compared to the pristine α-Fe_2O_3. The enhanced PEC performance of this ternary photoanode system was attributed to the formation of a type II heterojunction band alignment at the α-Fe_2O_3/B-C_3N_4 interface, effectively enhancing charge separation and increasing carrier density. Comprehensive characterizations revealed that p-CNT played a pivotal role in facilitating efficient electron transfer to the counter electrode, minimizing the recombination of photogenerated electron–hole pairs, and accelerating the oxygen evolution reaction. This research underscores the significance of the Z-scheme structure promoted by the synergistic effects of B-C_3N_4 and p-CNT, exemplifying pyrolytic carbon nanotubes as a cost-effective and versatile conductive material for PEC heterojunctions. This approach holds promise for achieving high-performance photoanodes in analogous semiconductor photocatalytic systems, thereby providing new opportunities in the realm of PEC water splitting.

Conflicts of interest

There are no conflicts to declare.

Acknowledgements

This work was supported by the National Research, Development and Innovation (NRDI) Fund of Hungary (Hungary) (grant numbers NKFI-128841, TKP2021-NKTA-05, K146032) and our research collaborators from IRCRE, Xi'an, China. This research was supported by grant no. VEKOP-2.3.3-15-2016-00002 and VEKOP-2.3.2-16-2016-00011 of the European Structural and Investment Funds. We gratefully acknowledge the assistance of Illés Levente, Kovács Zoltán (SEM) and Kornél Fél (ATR IR). We also thank the Renewable Energy National Laboratory (Hungary) for support, financed by the RRF-2.3.1-21-2022-00009 project.

References

1 T. H. Jeon, M. S. Koo, H. Kim and W. Choi, *ACS Catal.*, 2018, **8**, 11542–11563.
2 Z. Wang, C. Li and K. Domen, *Chem. Soc. Rev.*, 2019, **48**, 2109–2125.
3 T. Hisatomi, J. Kubota and K. Domen, *Chem. Soc. Rev.*, 2014, **43**, 7520–7535.
4 A. Landman, H. Dotan, G. Shter, *et al.*, *Nat. Mater.*, 2017, **16**, 646–651.
5 J. M. Mayer, *Annu. Rev. Phys. Chem.*, 2004, **55**, 363–390.
6 Z. W. Seh, J. Kibsgaard, C. F. Dickens, I. Chorkendorff, J. K. Nørskov and T. F. Jaramillo, *Science*, 2017, **355**, eaad4998.

7 J. Li, W. Wan, C. A. Triana, H. Chen, Y. Zhao, C. K. Mavrokefalos and G. R. Patzke, *Nat. Commun.*, 2021, **12**, 255.
8 M. Tahir, L. Pan, F. Idrees, *et al.*, *Nano Energy*, 2017, **37**, 136.
9 A. Liao, H. He, Y. Zhou and Z. Zou, *J. Semicond.*, 2020, **41**, 091709.
10 X. Yang, L. Tian, X. Zhao, *et al.*, *Appl. Catal., B*, 2019, **244**, 240–249.
11 A. U. Pawar, C. W. Kim, M. J. Kang and Y. S. Kang, *Nano Energy*, 2016, **20**, 156–167.
12 S. Bai, X. Yang, C. Liu, *et al.*, *ACS Sustain. Chem. Eng.*, 2018, **6**, 12906–12913.
13 T. Benkó, S. Shen, M. Németh, *et al.*, *Appl. Catal., A*, 2023, **145**, 1686–1695.
14 A. G. Tamirat, J. Rick, A. A. Dubale, W.-N. Su and B.-J. Hwang, *Nanoscale Horiz.*, 2016, **1**, 243.
15 S. Shen, S. A. Lindley, X. Chen and J. Z. Zhang, *Energy Environ. Sci.*, 2016, **9**, 2744.
16 J. L. Shelton and K. E. Knowles, *J. Phys. Chem. Lett.*, 2021, **12**, 3343–3351.
17 J. Zhang, J. Cui and S. Eslava, *Adv. Energy Mater.*, 2021, **11**, 2003111.
18 J. H. Kennedy and K. W. Frese Jr, *J. Electrochem. Soc.*, 1978, **125**, 709.
19 L. Li, Y. Yu, F. Meng, *et al.*, *Nano Lett.*, 2012, **12**, 724–731.
20 P. Tang and J. Arbiol, *Nanoscale Horiz.*, 2019, **4**, 1256.
21 B. Eftekharinia, A. Moshaii, N. S. Vayghan and A. Dabirian, *ChemCatChem*, 2018, **10**, 4665–4675.
22 C. C. Li, A. Li, Z. B. Luo, *et al.*, *Angew. Chem., Int. Ed.*, 2017, **56**, 4150–4155.
23 D. Wu and Z. Zhang, *Electrochim. Acta*, 2018, **282**, 48–55.
24 L. Wang, N. T. Nguyen, Z. Q. Shen, *et al.*, *Nano Energy*, 2018, **50**, 331–338.
25 K. Dang, T. Wang, C. Li, *et al.*, *Engineering*, 2017, **3**, 285–289.
26 Q. Guo, Q. Zhao, R. Crespo-Otero, *et al.*, *J. Am. Chem. Soc.*, 2023, **145**, 1686–1695.
27 W. Shi, C. Liu, M. Li, *et al.*, *J. Hazard. Mater.*, 2020, **389**, 121907.
28 Z. J. Wang, H. Xie, S. C. Jun, J. Li, L. C. Wei, Y. C. Fang, S. Liu, M. Ma and Z. Xing, *Mater. Horiz.*, 2024, **11**, 1808–1816.
29 M. Huang, T. Wang, Z. Wu, *et al.*, *J. Colloid Interface Sci.*, 2022, **628**, 129–140.
30 H. Guo, M. Chen, Q. Zhong, *et al.*, *J. CO2 Util.*, 2019, **33**, 233–241.
31 S. Liu, S. Wang, Y. Jiang, *et al.*, *Chem. Eng. J.*, 2019, **373**, 572–579.
32 L. Wang, W. Si, Y. Tong, *et al.*, *Carbon Energy*, 2020, **2**, 223–250.
33 M. Volokh, G. Peng, J. Barrio and M. Shalom, *Angew. Chem., Int. Ed.*, 2019, **58**, 6138–6151.
34 X. She, J. Wu, H. Xu, *et al.*, *Adv. Energy Mater.*, 2017, **7**, 1700025.
35 M. S. Nasir, G. Yang, I. Ayub, *et al.*, *Appl. Catal., B*, 2019, **257**, 117855.
36 N. Lei, J. Li, Q. Song and Z. Liang, *Int. J. Hydrogen Energy*, 2019, **44**, 10498–10507.
37 W. Kong, X. Zhang, B. Chang, *et al.*, *Electrochim. Acta*, 2018, **282**, 767–774.
38 S. Thaweesak, S. Wang, M. Lyu, *et al.*, *Dalton Trans.*, 2017, **46**, 10714–10720.
39 L. Mao, H. Deng, M. Li and S. Shen, *Sci. China Mater.*, 2023, **66**, 603–613.
40 A. Mehtab and T. Ahmad, *ACS Catal.*, 2024, **14**, 691–702.
41 A. Mehtab, S. A. Ali, P. P. Ingole, Y. Mao, S. M. Alshehri and T. Ahmad, *ACS Appl. Energy Mater.*, 2023, **6**, 12003–12012.
42 A. Mehtab, P. P. Ingole, J. Ahmed, Y. Mao and T. Ahmad, *J. Phys. Chem. C*, 2024, **128**, 85–94.
43 A. Mehtab, Y. Mao, S. M Alshehri and T. Ahmad, *J. Colloid Interface Sci.*, 2023, **652**, 1467–1480.
44 F. C. Pan, J. Jia, F. Gong, Y. Liu, S. Liu, S. C. Jun, D. Lin, Y. Guo, Y. Yamauchi and Y. Huo, *ACS Nano*, 2024, **18**, 6202–6214.
45 A. Mahmood, T. Muhmood and F. Ahmad, *Mater. Chem. Phys.*, 2022, **278**, 125640.
46 A. Horváth, M. Németh, A. Beck, G. Sáfrán, Z. E. Horváth, I. Rigó, Z. May and T. I. Korányi, *Appl. Catal., A*, 2024, 119651.
47 D. Zhao, Y. Wang, C.-L. Dong, Y.-C. Huang, J. Chen, F. Xue, S. Shen and L. Guo, *Nat. Energy*, 2021, **6**, 388–397.
48 D. Zhao, C. L. Dong, B. Wang, C. Chen, Y. C. Huang, Z. Diao, S. Li, L. Guo and S. Shen, *Adv. Mater.*, 2019, **31**, e1903545.
49 E. Wierzyńska, K. Korytkowska, K. Kazimierczuk, T. Łęcki, K. Zarębska, K. P. Korona, M. Pisarek, B. Furtak and M. Skompska, *J. Phys. Chem. C*, 2024, **128**, 894–907.
50 L. Chen, Y. Wang, S. Cheng, X. Zhao, J. Zhang, Z. Ao, C. Zhao, B. Li, S. Wang, S. Wang and H. Sun, *Appl. Catal., B*, 2022, **303**, 120932.
51 Q. Han, F. Zhao, C. Hu, *et al.*, *Nano Res.*, 2015, **8**, 1718–1728.
52 X. Shi, L. Cai, M. Ma, X. Zheng and J. H. Park, *ChemSusChem*, 2015, **8**, 3192–3203.
53 S. J. Clark, M. D. Segall, C. J. Pickard, P. J. Hasnip, M. J. Probert, K. Refson and M. C. Payne, *Z. Kristallogr.*, 2005, **220**, 567–570.
54 J. P. Perdew, K. Burke and M. Ernzerhof, *Phys. Rev. Lett.*, 1996, **77**, 3865–3868.
55 D. Vanderbilt, *Phys. Rev. B: Condens. Matter Mater. Phys.*, 1990, **41**, 7892–7895.
56 A. Tkatchenko and M. Scheffler, *Phys. Rev. Lett.*, 2009, **102**, 073005.
57 P. Biswas, A. Ainabayev, A. Zhussupbekova, F. Jose, R. O'Connor, A. Kaisha, B. Walls and I. V. Shvets, *Sci. Rep.*, 2020, **10**, 7463.
58 N. Bhandary, A. P. Singh, P. P. Ingole and S. Basu, *ChemPhotoChem*, 2016, **1**, 70–75.
59 Y. Liu, D.-P. Wang, Y.-X. Yu and W.-D. Zhang, *Int. J. Hydrogen Energy*, 2012, **37**, 9566–9575.
60 V. D. Dang, T. Annadurai, A. P. Khedulkar, J. Y. Lin, J. Adorna, W. J. Yu, B. Pandit, T. V. Huynh and R. A. Doong, *Appl. Catal., B*, 2023, **320**, 121928.
61 R. Chong, Z. Wang, J. Lv, J. Rong, L. Zhang, Y. Jia, L. Wang, Z. Chang and X. Wang, *J. Catal.*, 2021, **399**, 170–181.
62 S. Choudhury, U. Sahoo, S. Pattnayak, S. Padhiari, M. Tripathy and G. Hota, *New J. Chem.*, 2022, **46**, 13100.

63 T. Jeon, C. Park, U. Kang, G. Moon, W. Kim and H. Park, *Appl. Catal., B*, 2024, **340**, 123167.
64 Z. Pan, G. Zhang and X. Wang, *Angew. Chem., Int. Ed.*, 2019, **131**, 7176–7180.
65 C. Wang, S. Wei, F. Li, *et al.*, *Nanoscale*, 2020, **12**, 3259–3266.
66 J. Bai, H. Xu, G. Chen, *et al.*, *Mater. Chem. Phys.*, 2019, **7**, 9709–9718.
67 R. C. Pawar, Y. Pyo, S. H. Ahn and C. S. Lee, *Appl. Catal., B*, 2015, **176–177**, 654–666.
68 M. Benedet, D. Barreca, G. A. Rizzi, C. Maccato, J. L. Wree, A. Devi and A. Gasparotto, *Surf. Sci. Spectra*, 2023, **30**, 024021.
69 H. M. Banbela, L. M. Alharbi, R. H. Al-Dahiri, M. Jaremko and M. A. Salam, *Molecules*, 2022, **27**, 2708.
70 J. Li, N. Lei, H. Hao and J. Zhou, *Chem. Phys. Lett.*, 2017, **672**, 99–104.
71 X. Guo, L. Rao, P. Wang, L. Zhang and Y. Wang, *Int. J. Environ. Res. Public Health*, 2019, **16**, 581.
72 S. C. Yan, Z. S. Li and Z. G. Zou, *Langmuir*, 2010, **26**, 3894–3901.
73 B. Choudhury, K. K. Paul, D. Sanyal, A. Hazarika and P. K. Giri, *J. Phys. Chem. C*, 2018, **122**, 9209–9219.
74 M. Majdoub, Z. Anfar and A. Amedlous, *ACS Nano*, 2020, **14**, 12390–12469.
75 J. Deng, Q. Zhang, K. Feng, H. Lan, J. Zhong, M. Chaker and D. Ma, *ChemSusChem*, 2018, **11**, 3783–3789.
76 A. Thomas, A. Fischer, F. Goettmann, M. Antonietti, J.-O. Müller, R. Schlögl and J. M. Carlsson, *J. Mater. Chem.*, 2008, **18**, 4893–4908.
77 J. Qin, Y. Jiao, M. Liu, Y. Li and J. Wang, *J. Alloys Compd.*, 2022, **898**, 162846.
78 J. Meng, X. Zhang, Y. Liu, M. Ren, Y. Guo, X. Yang and Y. Yang, *Sci. Total Environ.*, 2021, **796**, 148946.
79 Y. Zhang, J. Yang, Z. Yu, Y. Hou, R. Jiang, J. Huang, F. Yang, S. Yao, L. Gao and W. Tang, *Chem. Eng. J.*, 2021, **416**, 129124.
80 C. Song and S. Kim, *J. Electrochem. Soc.*, 2015, **162**, F1181.
81 J. Hu, P. Zhang, W. An, L. Liu, Y. Liang and W. Cui, *Appl. Catal., B*, 2019, **245**, 130–142.
82 B.-Y. Geng, D. Chen, N. Li, Q. Xu, H. Li, J. He and J. Lu, *Appl. Catal., B*, 2021, **280**, 119409.
83 A.-M. W. Kadi, R. M. Mohamed, A. A. Ismail and D. W. Bahnemann, *Ceram. Int.*, 2020, **46**, 23098–23106.
84 T. Benkó, S. Shen, M. Németh, D. Lukács, Y. Xu, I. Khan, Z. Czigány, Z. E. Horváth, Z. Kovács, J. Su and J. S. Pap, *ChemElectroChem*, 2024, e202400191.
85 A. Tamirat, J. Rick, A. A. Dubale, W.-N. Su and B. J. Hwang, *Nanoscale Horiz.*, 2016, **1**, 243–267.
86 M. Li, T. Liu, Y. Yang, W. Qiu, C. Liang, Y. Tong and Y. Li, *ACS Energy Lett.*, 2019, **4**, 1983–1990.
87 S. Zhang, P. Shangguan, S. Tong, Z. Zhang and W. Leng, *J. Phys. Chem. C*, 2019, **123**, 24352–24361.
88 N. A. Arzaee, M. F. M. Noh, N. S. H. Mohd Ita, N. A. Mohamed, S. N. F. Mohd Nasir, I. N. N. Mumthas, A. F. Ismail and M. A. M. Teridi, *Dalton Trans.*, 2020, **49**, 11317–11328.
89 Q. Xu, B. Zhu, C. Jiang, B. Cheng and J. Yu, *Sol. RRL*, 2018, **2**, 1800006.
90 F. Ge, X. Li, M. Wu, H. Ding and X. Li, *RSC Adv.*, 2022, **12**, 8300–8309.
91 X. Chen, J. Wang, Y. Chai, Z. Zhang and Y. Zhu, *Adv. Mater.*, 2021, **33**, 2007479.
92 B. Duan and L. Mei, *J. Colloid Interface Sci.*, 2020, **575**, 265–273.
93 F. Li and B. Dong, *Ceram. Int.*, 2017, **43**, 16007–16012.
94 M. Joseph, M. Kumar, S. Haridas, C. Subrahmanyam and S. N. Remello, *Energy Adv.*, 2024, **3**, 30–59.